CrossMark

A Comparative Investigation on the Structural, Optical and Electrical Properties of SiO$_2$–Fe$_3$O$_4$ Core–Shell Nanostructures with Their Single Components

Neena Bachan[1] · A. Asha[2] · W. Jothi Jeyarani[1] · D. Arun Kumar[3] · J. Merline Shyla[1]

Abstract The SiO$_2$–Fe$_3$O$_4$ core–shell nanostructures were synthesized by sol–gel chemistry. The morphological features of the nanostructures were examined by field emission scanning electron microscopy which revealed the core–shell nature of the nanoparticles. X-ray diffraction studies evidenced the formation of SiO$_2$–Fe$_3$O$_4$ core–shell nanostructures with high degree of homogeneity. The elemental composition of the SiO$_2$–Fe$_3$O$_4$ core–shell nanostructures was determined by energy-dispersive X-ray spectroscopy analysis. Fourier transform infrared spectroscopy showed the Si–O–Fe stretching vibrations. On analysis of the optical properties with UV–Vis spectra and Tauc's plot, it was found that the band gap of SiO$_2$–Fe$_3$O$_4$ core–shell nanostructures diminished to 1.5 eV. Investigation of the electrical properties of the core–shell nanostructures using field-dependent conductivity measurements presented a significant increase in photoconductivity as compared to those of its single components, thereby rendering them as promising candidates for application as photoelectrodes in dye-sensitized solar cells.

KEY WORDS: Nanostructures; Sol–gel chemistry; Optical properties; X-ray diffraction; Electrical properties

1 Introduction

Recently, nanostructured materials have received considerable attention due to their intriguing physical and chemical properties with wide range of applications in various fields [1, 2]. Core–shell nanostructures constitute an important group of nanomaterials. Nanoshell particles

✉ J. Merline Shyla
   jmshyla@gmail.com

1   Department of Physics, Energy NanoTechnology Centre (ENTeC), Loyola Institute of Frontier Energy (LIFE), Loyola College, Chennai 600 034, India

2   Department of Physics, Dhanalakshmi Srinivasan College of Engineering and Technology, Chennai 603 104, India

3   Department of Physics, Shri Andal Alagar College of Engineering, Chennai 600 026, India

are highly functional materials with tailored properties, which are quite different than either of the core or the shell material. Indeed, they show modified and improved properties than their single-component counterparts or nanostructures of the same size. Therefore, nanoshell structures are preferred over nanostructures. Their properties can be modified by changing either the constituting materials or core-to-shell ratio [3]. Core–shell nanostructures of metal oxide semiconductors (MOS) have attracted much attention because of their most fascinating tunable applications. Enhancement of quantum yield observed in such structures was attributed to effective passivation of surface traps by formation of the shell [4], whose thickness is an important parameter in manipulating optical properties [5]. Other than enrichment of optical properties, core–shell nanostructures show very high reactivity in photochemical reactions compared to core nanoparticles [6, 7]. Silica nanoparticles are commonly used as core material to host guest shell structures [8]. In recent years, synthesis and

characterization of Fe_3O_4 nanoparticles (NPs) have been reported and used in various fields, such as information storage [9], drug delivery and targeting [10], and magnetic separation, because of their magnetic and electrochemical properties [11]. These magnetic nanoparticles have a large specific surface area [12] that can be effectively modified to attach dye molecules in dye-sensitized solar cells (DSSCs). The literature reveals increasing interest in new designs of the core–shell configurations such as SiO_2–ZrO_2 [13], SiO_2–TiO_2 [14], Fe_3O_4–SiO_2 [15, 16], SiO_2–poly-pyrrole [17], FePt–Fe_3O_4 [18], α-Fe_2O_3/Fe_3O_4 [19] and so on. SiO_2–Fe_3O_4 is a type II core–shell nanoparticle where the narrow band gap shell material is grown over the wider band gap core material. The enhanced control over carrier distribution afforded by materials proves useful for many applications, such as photovoltaic and photoconduction devices [20]. The synthesis procedure plays a crucial role in controlling the size and shape of the nanostructure and hence detecting different properties of the material [21]. The sol–gel technology is very efficient in producing various functional materials in which particle size, porosity, thin layer thickness, separation of particles with different composition and structures may be controlled, thereby leading to successful applications [22]. The key objectives of the work were to synthesize SiO_2–Fe_3O_4 core–shell nanoparticles and their single components by sol–gel route to study the surface morphology, phase identification, chemical bonds and structure, and optical absorption properties of the as-synthesized samples using FE-SEM, XRD, FTIR and UV–visible spectroscopy, respectively, and to record and analyze the photoconducting property of the samples in order to determine their suitability as electrodes in solar cell applications.

Though there have been several reports on core–shell nanostructures, the present work, wherein SiO_2 core particles were coated with a Fe_3O_4 shell layer using the sol–gel approach, is a novel nanosystem ever attempted before. The field-dependent dark and photoconducting nature of the core–shell nanoparticles which is seldom probed provided important insights into the transport behavior of the system favouring an increase in the photoinduced current, for possible photovoltaic applications. The findings reported herein gain significance as certain unique associations between key parameters of the nano-core–shell system such as morphology, size, energy gap and optoelectrical properties have been established with them.

2 Experimental

The sol–gel process is a bottom–up, wet-chemical technique widely used in material research related to science and technology applications, in particular for metal oxide nanoparticle synthesis. This process is a combination of two steps, hydrolysis and polycondensation of suitable molecular precursors (usually metal alkoxides or chlorides), which leads to the gradual formation of the solid-phase network [23]. The main benefits of sol–gel chemistry are the high purity and uniformity of nanostructures achievable at low temperatures and the possibility of using different precursors [24].

2.1 Synthesis of SiO_2 and Fe_3O_4 Nanoparticles

Monodispersed spherical SiO_2 core nanoparticles were synthesized by sol–gel method. The solution of tetraethyl orthosilicate Si $(OC_2H_5)_4$, which is the precursor, was added dropwise into the solvent isopropyl alcohol and stirred for 30 min. Hydrolysis of the precursor resulted in the formation of hydrated silicon hydroxide which subsequently undergoes condensation to form –Si–O–Si– bonds. The rate of hydrolysis was minimal at neutral pH, and as the pH increased, rate of hydrolysis also increased and so dropwise addition of 1 mol NH_3 solution was done under stirring. When sufficient Si–O–Si bonds were formed in a region, the sol formation occurred. With time, the sol and condensed species link together to form a three-dimensional network and gelation happens. The resultant solution was stirred for 24 h and kept for 1-day aging and then filtered in order to remove any particulates. The precipitate was washed several times with distilled water and dried in oven for 24 h to remove the solvent. Removal of residual organics and the stabilization of the materials were done by calcination for 4 h at 400 °C [25, 26]. In the same manner, Fe_3O_4 nanoparticles were synthesized by changing the precursor to anhydrous ferric chloride ($FeCl_3$).

2.2 Synthesis of SiO_2–Fe_3O_4 Core–shell Nanoparticles

The synthesis of SiO_2–Fe_3O_4 nanoparticles was carried out in the manner as described below using sol–gel method. The silicon dioxide nanoparticles synthesized by the above procedure were dispersed in isopropyl alcohol, and a solution of ferric chloride in isopropyl alcohol was added to the above reaction medium dropwise and stirred for 30 min in order to form Fe_3O_4 shell over SiO_2 core nanoparticles. While stirring, 1 mol NH_3 was added to get the mixed oxide gel. The resultant solution was stirred for 24 h, and the precipitate was washed several times in distilled water and annealed at 400 °C. An illustrative representation of the reaction mechanism of formation of core–shell along with consecutive steps is presented in Fig. 1. The attractive electrostatic forces between the non-functionalized silica and ferrite particles are strong, and thus Fe_3O_4 was stably assembled over SiO_2 core [27].
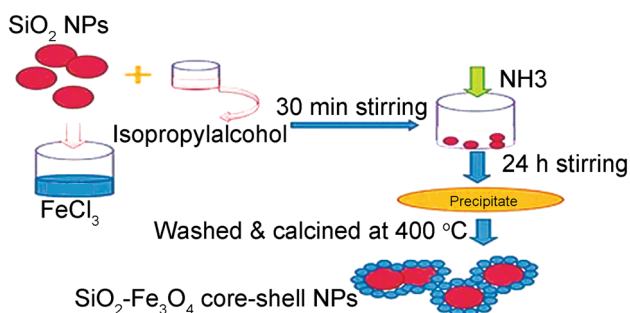
Fig. 1 Illustrative representation of SiO$_2$–Fe$_3$O$_4$ core–shell formation

2.3 Characterization

The field emission scanning electron micrographs of pure SiO$_2$, Fe$_3$O$_4$ and SiO$_2$–Fe$_3$O$_4$ core–shell nanoparticles have been recorded using the field emission scanning electron microscope (FE-SEM) Quanta 200 FEI—Netherland, equipped with an EDS system for morphological studies. The crystal structure of the as-synthesized samples was studied by X-ray diffraction and has been recorded by the powder diffraction method using Rich Siefert 3000 X-ray diffraction equipped with a CuK_α monochromatic radiation source ($\lambda = 1.54187$ Å) over the 2θ range from 10°–90° at the rate of 2.5°/min. The Fourier transform infrared spectra of the samples were studied using PerkinElmer infrared spectrophotometer. The spectra were recorded in the wavenumber range of 500–4000 cm^{-1}. The optical absorption spectra were recorded in the range 190–1100 nm using Lambda-35-UV spectrometer. The field-dependent dark and photoconductivity studies were carried out using Keithley Picoammeter 6485. The experimental setup for the measurement of field-dependent dark and photoconductivity was as described in Ponniah et al. [28]. The samples in the form of pellets were attached to the microscopic glass slide, and two electrodes of thin copper wire (0.14 mm diameter) were fixed by the use of silver paint. The ends of the copper wire were connected to DC power supply through picoammeter, the applied field was varied, and the corresponding current in the circuit was measured. To measure the photocurrent, light from a 100 W Halogen lamp was illuminated onto the sample, and the measurements were repeated.

3 Results and Discussion

During the sol–gel process, Fe$_3$O$_4$ was generated by the hydrolysis and condensation of the precursor ferric chloride and then deposited on SiO$_2$ core particle to form a shell layer. Significant changes in the properties of the core were detected after being coated with the shell material which was studied using the standard characterization techniques.

3.1 Microscopic Analysis

Figure 2a shows the FE-SEM image of SiO$_2$ nanoparticles. The nanoparticles were found to be uniquely spherical in shape and uniformly distributed. The particle size of the SiO$_2$ nanoparticles was found to be diameter of 800 nm and in agreement with reported results [29]. A high amount of porosity was observed in the SiO$_2$ nanoparticles. Figure 2b shows the FE-SEM image of the pure Fe$_3$O$_4$ nanoparticles, which are nanoporous. The surfaces of the Fe$_3$O$_4$ nanoparticles were noticeably rough, and the porosity further increased the roughness of the Fe$_3$O$_4$ surface. In the FE-SEM image of the Fe$_3$O$_4$ microspheres, there were many nearly monodisperse microspheres with diameters of about 46–75 nm. The Fe$_3$O$_4$ nanoparticles were agglomerated as these magnetic nanoparticles generally incline to merge toward each other due to the magnetic dipole interaction between them [30]. The control of the monodisperse size is very important because the properties of nanocrystal strongly depend upon the dimension of nanoparticles [31]. Figure 2c shows the FE-SEM micrographs of the synthesized SiO$_2$–Fe$_3$O$_4$ core–shell nanoparticles. From the figure, approximately spherical morphology was apparent, which clearly exhibited the formation of SiO$_2$–Fe$_3$O$_4$ core–shell nanostructure with scantily observed agglomeration of the shell material in certain areas that could have occurred in order to minimize the total surface energy of the system due to large surface-to-volume ratio and strong magnetic attraction forces that existed in Fe$_3$O$_4$ nanoparticles. The core appeared darker in contrast to the shell due to the difference in electron penetration efficiency [30]. The smooth surface of SiO$_2$ core particles was roughened due to the deposition of Fe$_3$O$_4$ nanoparticles, and the shell formation around silica core was visible. The diameters ranged from about 14 to 67 nm and are almost similar to that of the shell material. This could be due to the coating of shell material, and the particle size observed therein probably corresponded to that of the shell rather than the core–shell nanostructure.

Figure 3 shows the EDS spectra of Fe$_3$O$_4$ and SiO$_2$–Fe$_3$O$_4$ core–shell nanostructures. The EDS spectrum of Fe$_3$O$_4$ asserted the presence of Fe element alone in the sample which was indicative of the purity of the as-synthesized sample (Fig. 3a). Figure 3b confirms the presence of Si and Fe and a small amount of Cl impurity. Shell coating was evident from the changes in size, shape and the presence of Fe in the elemental composition as determined from EDS. The presence of Si peaks further indicated the manifestation of SiO$_2$ as core in the as-synthesized sample.

3.2 Scattering Analysis

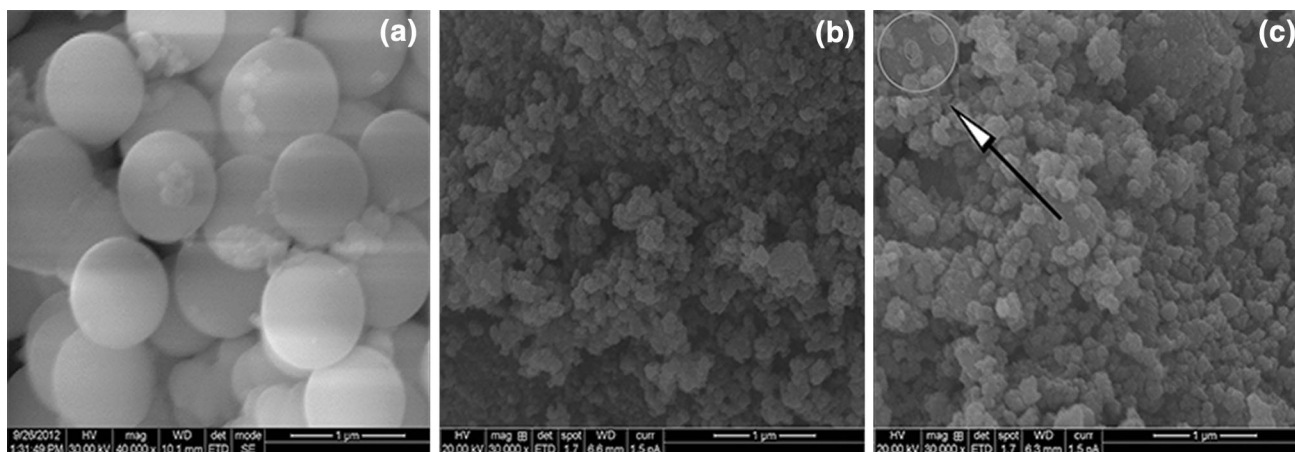Figure 4 shows the XRD pattern of SiO$_2$ nanostructures, which was in good agreement with the standard ICDD No:

Fig. 2 FE-SEM images of SiO$_2$ **a**, Fe$_3$O$_4$, **b** SiO$_2$–Fe$_3$O$_4$ core–shell **c** nanoparticles
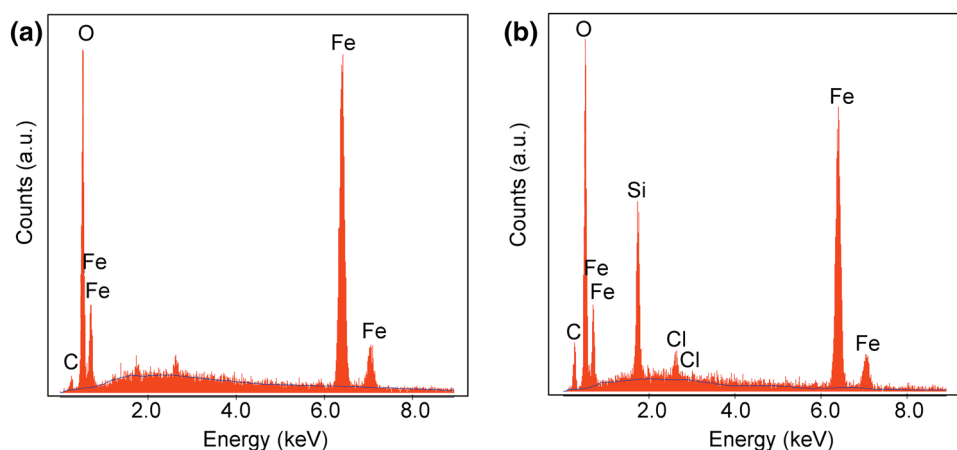
Fig. 3 EDS spectra of Fe$_3$O$_4$ nanoparticles **a**, SiO$_2$–Fe$_3$O$_4$ core–shell nanoparticles **b**
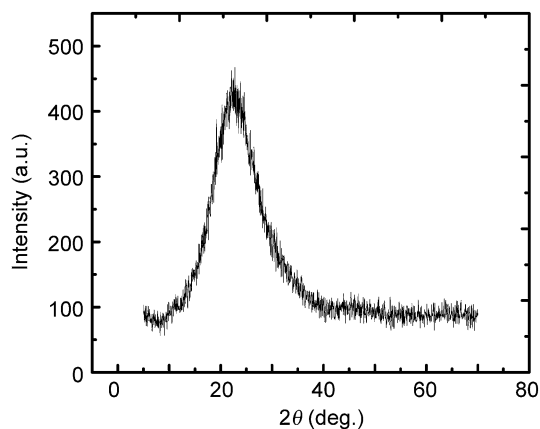

Fig. 4 XRD pattern of SiO$_2$ nanoparticles

29-0085. The XRD pattern of SiO$_2$ nanoparticles showed the presence of a broad peak centered at 22° which indicated the assembly of silica nanostructures and was in good

agreement with the literature [32]. The average crystallite size of SiO$_2$ nanoparticles was obtained by calculation using Scherrer's formula $D = 0.9\lambda/(\beta\cos\theta)$, where D is the particle size, λ is the X-ray wavelength (nm), θ is Bragg's angle, and β is full width at half maximum [33]. The broad peak also indicated that the particles are of either very small crystalline or semicrystalline nature of about 0.63 nm as reported in the earlier work [34]. The XRD pattern of the as-synthesized Fe$_3$O$_4$ nanostructures is shown in Fig. 5 agreed well with the standard diffraction card ICDD No: 75-0033, for Fe$_3$O$_4$ with the cubic inverse spinal structure displaying the typical peaks at 35°, 57°, 62° and 64° corresponding to (3 1 1), (5 1 1), (4 4 0) and (4 4 1) crystal planes, respectively, which is in good agreement with that in Ref. [35]. These peaks were quite identical when compared to the bulk XRD pattern of Fe$_3$O$_4$ (cubic) with ICDD No: 89-4319 [36]. The strong and sharp peaks suggested that the Fe$_3$O$_4$ nanoparticles were highly crystalline [37]. The crystallite size of Fe$_3$O$_4$ nanostructures was
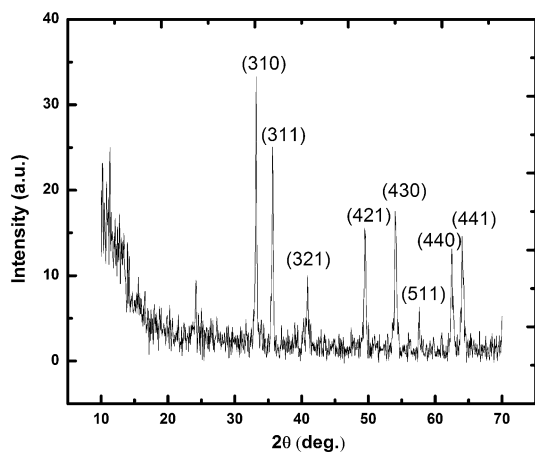
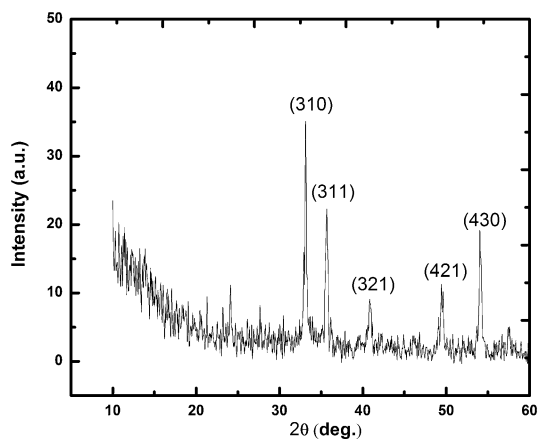Fig. 5 XRD pattern of Fe_3O_4 nanoparticles

Fig. 6 XRD pattern of SiO_2–Fe_3O_4 core–shell nanoparticles

determined to be about 14 nm. When compared to the bulk, the broad peaks also indicated the ultra-fine nature and small crystallite size of Fe_3O_4 nanoparticles [38]. In addition to the peaks of Fe_3O_4, some peaks of Fe_2O_3 corresponding to (310), (321), (421) and (430) planes were also found in the prepared sample which could not be excluded as both phases are very similar [39]. Figure 6 shows the XRD pattern of as-synthesized SiO_2–Fe_3O_4 core–shell nanostructures. It could be observed that the XRD pattern exhibited peaks at 32°, 35°, 40°, 49° and 54° corresponding to (310), (311), (321), (421) and (430) crystal planes, respectively. The results indicated the formation of SiO_2–Fe_3O_4 core–shell nanostructures and that the crystal structure of SiO_2 underwent a variation after being coated with Fe_3O_4. Because of the coating of the shell material, the diffraction peak intensity of amorphous SiO_2 which is the core material disappeared after and adequate thickness was laid down [17], confirming the complete formation of the shell over the SiO_2 core. Lattice parameters of core do not record any growth which could be an additional

contributory factor. The crystallite size measured using Scherrer's formula of the as-synthesized core–shell nanostructure from the XRD pattern was approximately 15 nm which was same as that of Fe_3O_4 shell as the high intensity from the diffraction peaks of core–shell indicated that the reflections are from the planes of Fe_3O_4 shell alone probably due to the optimal coating [40].

3.3 Spectroscopic Analysis

Fourier transform infrared (FTIR) technique gives a spectrum which represents the molecular absorption and transmission of infrared rays by the nanoparticles, creating a molecular fingerprint of the sample, and it shows common bands assigned to various vibrations in the solids nanostructures, respectively. Figure 7a shows the FTIR spectrum of SiO_2 nanoparticles. The two strong bands observed at 1118 and 804 cm^{-1} were associated with asymmetric and symmetric Si–O–Si stretching vibrations, respectively [41]. These confirmed that the SiO_2 phase was formed. Figure 7b shows the FTIR spectrum of the as-synthesized Fe_3O_4 nanostructures. The characteristic absorption peak of Fe_3O_4 was found at 459 and 555^{-1} which confirmed the Fe–O bending and stretching vibrations, respectively [42]. The peaks at 1621 cm^{-1} were assigned to O–H stretching vibrations [43, 44]. FTIR spectrum provides an additional proof for the formation of core–shell nanostructures with functionalized shells [45]. Figure 7c shows the FTIR spectrum of the as-synthesized SiO_2–Fe_3O_4 core–shell nanostructures. In the case of SiO_2–Fe_3O_4, the characteristic Fe–O peak shifted to 470.34 and 545 cm^{-1}, suggesting a chemical interaction between SiO_2 and Fe_3O_4. The peaks at 803 and 1095 cm^{-1} were assigned to symmetric and asymmetric stretching vibrations of Si–O, respectively [46]. After coating, the intensities of Si–O peaks reduced significantly, while the peaks at about 545 cm^{-1} which corresponded to the stretching vibrations of Fe–O were very pronounced in the core–shell sample, and this could be explained by the existence of higher portion of surface groups bounded to SiO_2. This could be due to the higher specific surface area and fine pore structure which originated from the nanoporous shell around the core particle [47]. The peak at 962 cm^{-1} indicated the Si–O–Fe stretching vibrations [48].

Optical properties are generally extremely sensitive to any nanocrystal surface modification. They can give indirect support about the coating of the shell materials on the core surface. The UV–visible spectrum of SiO_2 nanoparticles is shown in Fig. 8a. The absence of any absorption peak in the visible region of pure SiO_2 nanoparticles spectrum was in good agreement with the wide band gap nature of the material and its inability to absorb in the visible range. The optical band gap was estimated by
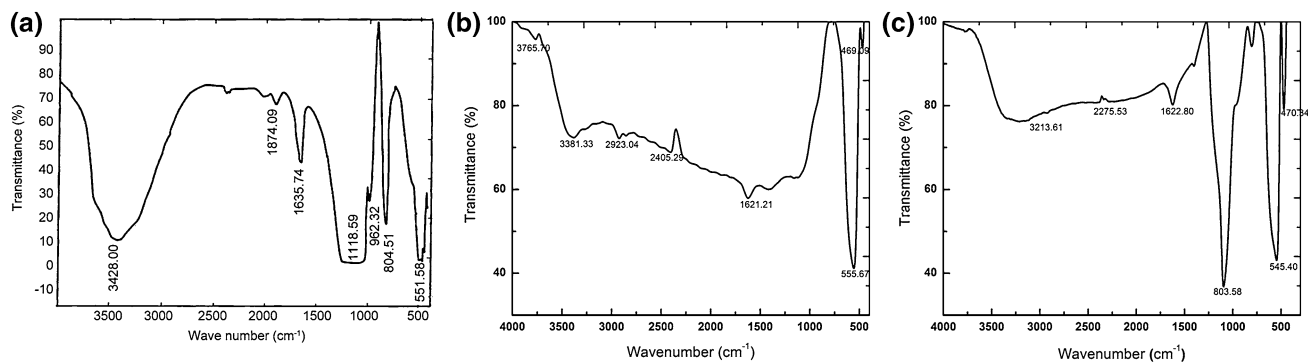
Fig. 7 FTIR spectra of SiO$_2$ nanoparticles **a**, Fe$_3$O$_4$ nanoparticles **b**, SiO$_2$–Fe$_3$O$_4$ core–shell nanoparticles **c**
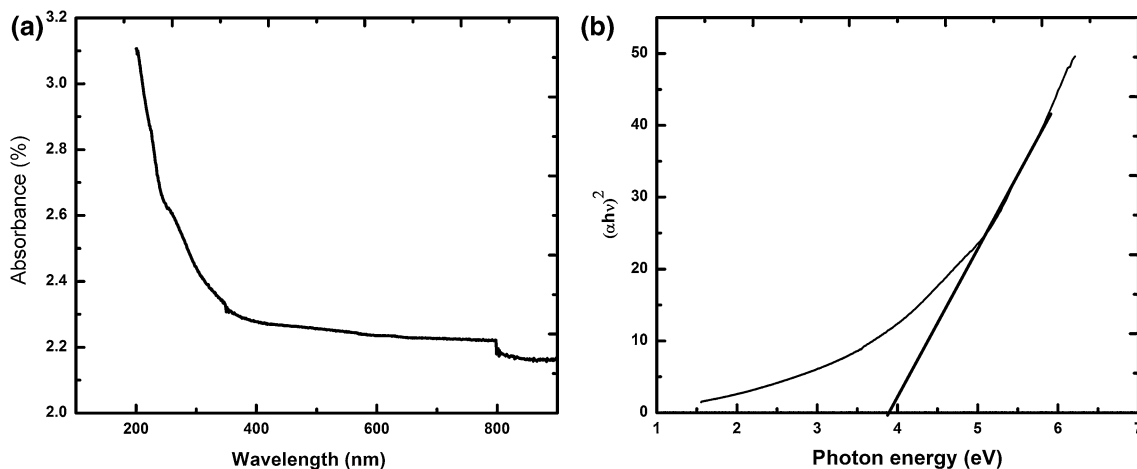

Fig. 8 UV spectrum **a**, optical band gap **b** of SiO$_2$ nanoparticles

plotting photon energy versus $(\alpha h v)^{2-}$ based on the relation $(\alpha h v)^2 = A(h v - E_g)$, where α is absorption coefficient, A is a constant, and E_g is the band gap [49, 50]. According to the above relation, the intercept of the tangent on the photon energy axis corresponds to the optical band gap and it was found to be 3.8 eV in the case of SiO$_2$ nanostructures from the Tauc's plot in Fig. 8b. The UV–visible spectrum of Fe$_3$O$_4$ nanostructures is shown in Fig. 9a. It shows an absorption band in the region of 200–455 nm, which originated primarily from the absorption and scattering of UV radiation by magnetic nanoparticles. The λ_{max} was found to be 455 nm. From the Tauc's plot in Fig. 9b, the optical band gap of Fe$_3$O$_4$ nanostructures was found to be 2.2 eV [51]. The UV–Vis spectrum and Tauc's plot of SiO$_2$–Fe$_3$O$_4$ core–shell nanostructures are shown in Fig. 10. The absorption bands were found in the region of 328–558 nm. The intensity and peak wavelength of absorbance changed after coating, and the wavelength shifted toward those of the pure shell materials, thus providing indirect support for the shell material coating on the core surface. It was found that the absorption peak at

558 nm revealed a redshift suggestive of a band gap reduction. The intensity of absorption was found to increase in the core–shell nanostructures when compared to SiO$_2$ and Fe$_3$O$_4$. From the Tauc's plot, the optical band gap of the core–shell nanostructures was found to be 1.5 eV. Thus, the optical band gap of the core–shell nanostructures decreased when compared to SiO$_2$ and Fe$_3$O$_4$. Table 1 shows the hierarchical order of the as-synthesized nanoparticle samples based on the band gap as obtained from their respective Tauc's plots. The SiO$_2$–Fe$_3$O$_4$ core–shell had the least band gap as compared to SiO$_2$ core and Fe$_3$O$_4$ shell. This strongly suggested the possibility of enhanced spectral response in the case of core–shells as compared to the SiO$_2$ and Fe$_3$O$_4$ nanostructures. Reduction in the band gap was correlated with increase in particle size which predicted the size-dependent energy gap [52].

3.4 Electrical Conductivity Analysis

The variation of dark and photoconductivity of SiO$_2$, Fe$_3$O$_4$ and SiO$_2$–Fe$_3$O$_4$ core–shell nanostructures is shown in
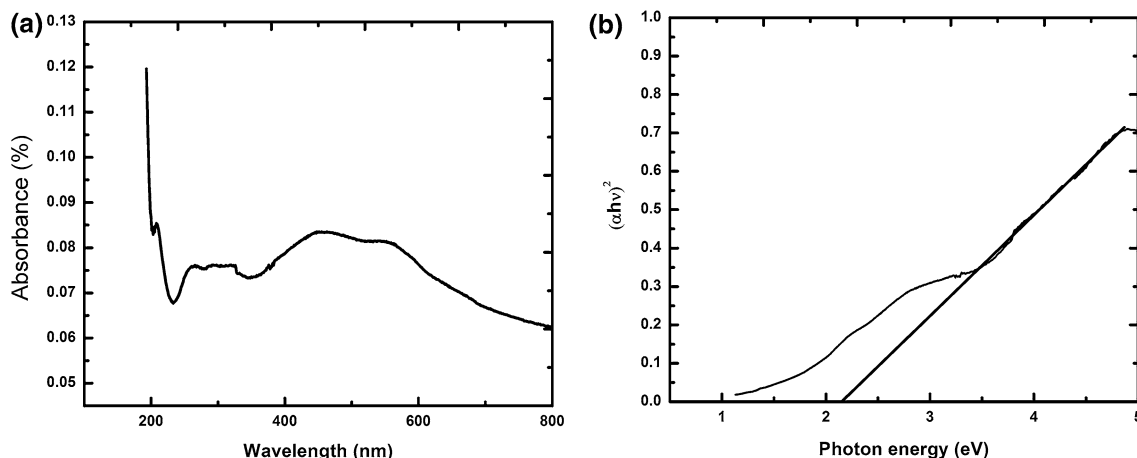
Fig. 9 UV spectrum **a**, optical band gap **b** of Fe_3O_4 nanoparticles
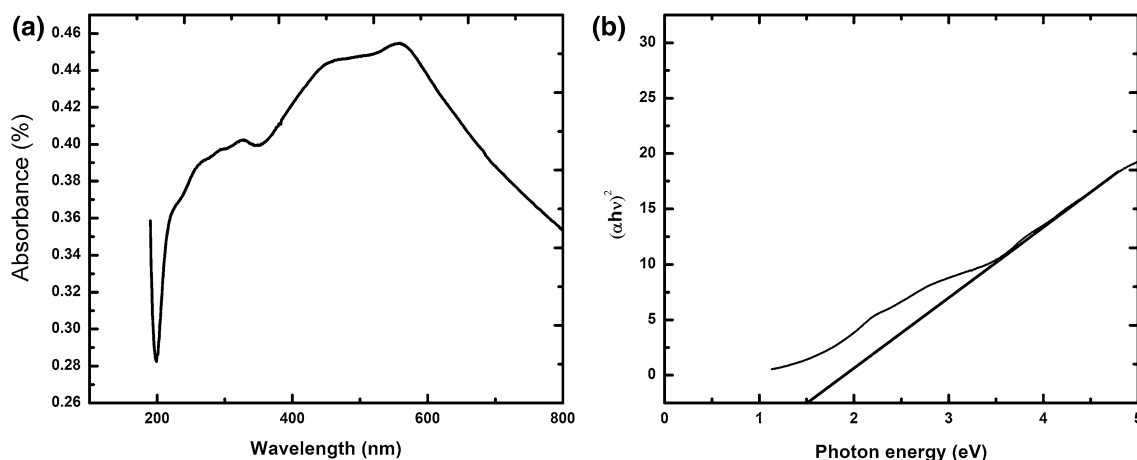

Fig. 10 UV spectrum **a**, optical band gap **b** of SiO_2–Fe_3O_4 core–shell nanoparticles

Table 1 Optical band gap of as-synthesized samples

SiO_2	Fe_3O_4	SiO_2–Fe_3O_4 core–shell
3.8 eV	2.2 eV	1.5 eV

Fig. 11. All the plots indicated linear increases in current in the dark and visible light-illuminated samples with increasing applied field, thereby depicting the ohmic nature of the contacts. The low values of dark current and insignificant rise in photocurrent upon visible light illumination were as expected. This is due to the wide band gaps of SiO_2, Fe_3O_4 and SiO_2–Fe_3O_4 core–shell nanostructures, qualifying them to absorb light of wavelengths below 400 nm only. For example, considering a fixed field 400 V/cm, the SiO_2, Fe_3O_4 and SiO_2–Fe_3O_4 core–shell nanostructures showed dark currents of 0.0021, 0.61 and 0.84 μA, respectively. When the light was switched on, the photocurrent initially increased very rapidly due to the quick generation of electron and hole pairs as a result of absorption of photons. For a fixed field of 400 V/cm SiO_2, Fe_3O_4 and SiO_2–Fe_3O_4 core–shell nanostructures showed photocurrents of 0.0031, 0.8 and 1.23 μA, respectively. In the case of SiO_2–Fe_3O_4 core–shell nanostructures, a significant increase in the dark and photocurrents by orders of about 4×10^2 and 4×10^3 times, respectively, was revealed when compared to SiO_2 nanostructures. However, the increase in the dark and photocurrents of the core–shell particles as compared to those of the Fe_3O_4 nanostructures was relatively lesser and was by orders of about 1.4- and 1.5-folds, respectively. Introduction of Fe_3O_4 decreased the energy barrier for conduction and increased the drift mobility of charge carriers, thereby elevating the conductivity and consequentially the mobility of holes acting as traps for electrons [53]. As the particle size decreased, there was an enhancement in surface area available for conduction, and therefore an increase in photocurrent
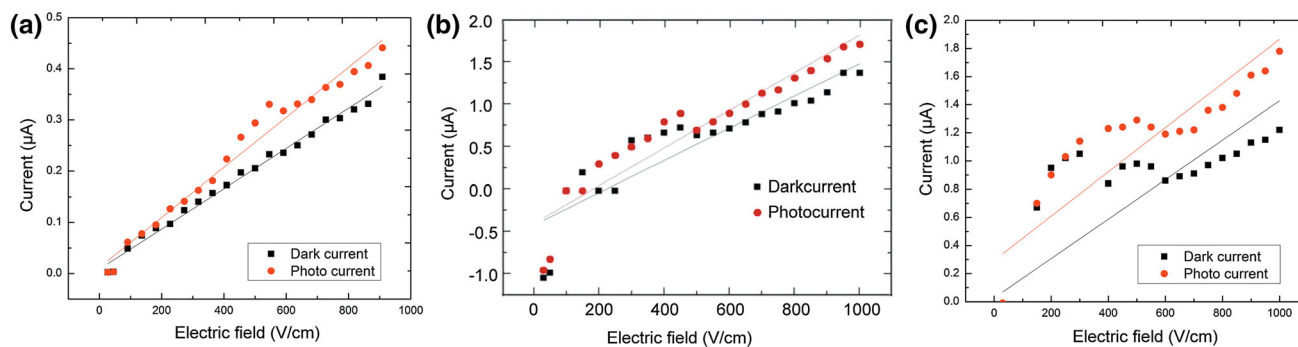
Fig. 11 Field-dependent conductivity of SiO₂ nanoparticles **a**, Fe₃O₄ nanoparticles **b**, SiO₂–Fe₃O₄ core–shell nanoparticles **c**

evidenced that the sample had acquired more photosensitivity [54]. Thus, the observed increase in dark and photocurrent of core–shell nanostructures was essentially due to the enhanced surface area available for conduction or due to the increase in charge carrier concentration [55]. Thus, it could be concluded that SiO₂–Fe₃O₄ core–shell nanostructures exhibited improved dark and photoconductivity in comparison with the SiO₂ and Fe₃O₄ nanostructures.

a reduction in the band gap as compared to SiO₂ and Fe₃O₄ and its single components and thus presenting them as promising candidates in the making of photoelectrodes for dye-sensitized solar cells.

4 Conclusions

SiO₂, Fe₃O₄ and SiO₂–Fe₃O₄ core–shell nanostructures were synthesized by the sol–gel method. Creation of metal oxide SiO₂–Fe₃O₄ core–shell nanostructures greatly enhanced the properties of the parent materials which were pure SiO₂ and Fe₃O₄ nanoparticles. FE-SEM images with EDS spectrum revealed the homogenous nature of the samples and uniform pore distribution on the surface. The XRD results indicated the formation of SiO₂–Fe₃O₄ core–shell nanostructures and that the crystal structure of SiO₂ experienced a variation after being coated with Fe₃O₄. The crystallite size calculated using Scherrer's formula was found to be in excellent agreement with the particle size inferred from the FE-SEM images. The FTIR spectrum indicated the Si–O–Fe stretching vibrations in the core–shells. The optical band gap of SiO₂–Fe₃O₄ core–shell nanostructures calculated using Tauc's plot was found to be 1.5 eV, which is significantly lesser than that of the individual SiO₂ and Fe₃O₄ nanoparticles which were 3.8 and 2.2 eV, respectively. Field-dependent photoconductivity measurements revealed an improved photoconductivity behavior in the case of core–shells in comparison with the SiO₂ and Fe₃O₄ nanoparticles. It could be concluded that the formation of SiO₂–Fe₃O₄ core–shell nanostructures was verified with various analysis tools and it was found to exhibit enhanced transport properties which could be attributed to the increased particle size, leading to

References

[1] Q.F. Zhang, G.Z. Cao, Nano Today **6**, 91 (2011)
[2] A. Rajesh, M. Manivel Raja, K. Gurunathan, Acta Metall. Sin. (Engl. Lett.) **27**, 253 (2014)
[3] K. Suchita, S.W. Gosavi, J. Urban, S.K. Kulkarni, Curr. Sci. **91**, 1038 (2006)
[4] A. Emamdoust, S.F. Shayesteh, M. Marandi, Pramana J. Phys. **80**, 713 (2012)
[5] B.O. Dabboussi, J. Rodriguez-Viejo, F.V. Mikulec, J.R. Heine, H. Mattoussi, R. Ober, K.F. Jensen, M.G. Bawendi, J. Phys. Chem. B **101**, 9463 (1997)
[6] M. Ethayaraja, C. Ravikumar, D. Muthukumaran, K. Dutta, R. Bandyopadhyaya, J. Phys. Chem. C **111**, 3246 (2007)
[7] K. Cendrowski, X. Chen, B. Zielinska, R.J. Kalenczuk, M.H. Rummeli, B. Buchner, R. Klingeler, E. Borowiak-Palen, J. Nanopart. Res. **13**, 5899 (2011)
[8] B.J. Li, H.Q. Cao, J. Shao, M.Z. Qu, J.H. Warner, J. Mater. Chem. **21**, 5069 (2011)
[9] T. Dung, T. Danh, L. Hoa, D.M. Chien, N.H. Duc, J. Exp. Nanosci. **4**, 259 (2009)
[10] P. Liu, W. Zhong, H. Shi, D. Xue, J. Exp. Nanosci. **4**, 323 (2009)
[11] M.E. Khosroshahi, L. Ghazanfari, M. Tahriri, J. Exp. Nanosci. **6**, 580 (2011)
[12] J.M. Kima, S.M. Changa, S. Kimb, K.S. Kimc, J. Kimb, W.S. Kimb, Ceram. Int. **35**, 1243 (2009)
[13] S. Son, S.H. Hwang, C. Kim, J.Y. Yun, J. Jang, A.C.S. Appl, Mater. Interfaces **5**, 4815 (2013)
[14] Y.J. Yao, S.D. Miao, S.M. Yu, L.P. Ma, H.Q. Sun, S.B. Wang, J. Colloid Interface Sci. **379**, 20 (2012)
[15] E.S. Jang, J. Korean Chem. Soc. **56**, 478 (2012)
[16] X.H. Liu, H.Y. Wu, F.L. Ren, G.Z. Qiu, M.T. Tang, Mater. Chem. Phys. **109**, 5 (2008)
[17] H. Zeng, J. Li, Z.L. Wang, J.P. Liu, S.H. Sun, Nano Lett. **4**, 187 (2004)

[18] Y. Tian, D. Wu, X. Jia, B.B. Yu, S.H. Zhan, J. Nanomater. **2011**, 5 (2011)

[19] S. Kim, B. Fisher, H.J. Eisler, M. Bawendi, J. Am. Chem. Soc. **125**, 11466 (2003)

[20] P. Mallick, S. Sahu, Nanosci. Nanotechnol. **2**, 71 (2012)

[21] Y. Dimitriev, Y. Ivanova, R. Iordanova, J. Univ. Chem. Technol. Metall. **43**, 181 (2008)

[22] R.G. Chaudhuri, S. Paria, Chem. Rev. **112**, 2373 (2012)

[23] S. Azimi, ISRN Nanotechnol. **2013**, 815071 (2013). doi:10.1155/2013/815071

[24] J. Aguado, R. van Grieken, M.J. López-Muñoz, J. Marugán, Appl. Catal. A **312**, 202 (2006)

[25] K.D. Arun, S.J. Merline, P.X. Francis, Appl. Nanosci. **2**, 429 (2012)

[26] Z. Libor, Q. Zhang, C. Israel, N.D. Mathur, Mater. Sci. Technol. **25**, 1307 (2009)

[27] D. Ponniah, F. Xavier, Phys. B **392**, 20 (2007)

[28] D.S. Yun, H.J. Kim, J.W. Yoo, Bull. Korean Chem. Soc. **26**, 1927 (2005)

[29] K.K. Siong, N.F. Amari, T.C. Yuan, S. Radiman, R. Yahaya, M.S. Yasir, Sains Malays. **42**, 167 (2013)

[30] L. Sophie, F. Delphine, P. Marc, R. Alain, R. Caroline, V.E. Luce, N.M. Robert, Chem. Rev. **108**, 2064 (2008)

[31] K.F. Yu, Y.P. Guo, X.F. Ding, J.Z. Zhao, Z.C. Wang, J. Mater. Lett. **59**, 4013 (2005)

[32] M.J. Chithra, M. Sathya, K. Pushpanathan, Acta Metall. Sin. (Engl. Lett.) **28**, 394 (2015)

[33] K.D. Arun, X.J. Alex, S.J. Merline, P.X. Francis, J. Mater. Sci. **48**, 3700 (2013)

[34] X.P. Zhang, W.Q. Jiang, X.L. Gong, Z. Zhang, J. Alloys Compd. **508**, 400 (2010)

[35] V. Subramanian, D.W. Jeong, W.B. Han, W.J. Janq, J.O. Shim, J.W. Bae, H.S. Roh, New J. Chem. **38**, 4872 (2014)

[36] O. ur Rahman, S.C. Mohapatra, S. Ahmad, Mater. Chem. Phys. **132**, 196 (2012)

[37] F. Gu, S.F. Wang, M.K. Lu, G.J. Zhou, D. Xu, D.R. Yuan, J. Phys. Chem. B **108**, 8119 (2004)

[38] F. Márquez, T. Campo, M. Cotto, R. Polanco, R. Roque, P. Fierro, J.M. Sanz, E. Elizalde, C. Morant, Soft Nanosci. Lett. **1**, 25 (2011)

[39] D.W. Wang, X.M. Zhu, S.F. Lee, H.M. Chan, H.W. Li, S.K. Kong, J.C. Yu, C.H.K. Cheng, K.C.F. Leung, J. Mater. Chem. B **1**, 2934 (2013)

[40] L.Y. Wang, J. Luo, Q. Fan, M. Suzuki, I.S. Suzuki, M.H. Engelhard, Y.H. Lin, N. Kim, J.Q. Wang, C.J. Zhong, J. Phys. Chem. B **109**, 21593 (2005)

[41] A.M. Awwad, N.M. Salem, Nanosci. Nanotechnol. **2**, 208 (2012)

[42] S.C.B. Myneni, S.J. Traina, G.A. Waychunas, T.J. Logan, Geochim. Cosmochim. Acta **62**, 3499 (1998)

[43] S. Vaidya, P. Thaplyal, A.K. Ganguli, Nanoscale Res. Lett. **6**, 169 (2011)

[44] N.R. Panda, D. Sahu, B.S. Acharya, P. Nayak, S.P. Pati, D. Das, Acta Metall. Sin. (Engl. Lett.) **27**, 563 (2014)

[45] J.S. Bhaskar, G. Parthasarathy, N.C. Sarmah, Bull. Mater. Sci. **31**, 775 (2008)

[46] M. Nikolić, K.P. Giannakopoulos, V.V. Srdić, Process. Appl. Ceram. **4**, 81 (2010)

[47] G.M. Jorge, V.A. Guadaluper, W.G. Raúl, L.P.M. José, M. Vivianne, J. Nanosci. Nanotechnol. **8**, 1 (2008)

[48] M.I. Amal, K.H. Kim, Chalcogenide Lett. **9**, 345 (2012)

[49] H.S. Al-Salman, M.J. Abdullah, Acta Metall. Sin. (Engl. Lett.) **28**, 230 (2015)

[50] A.A. Yelil, M. Hema, P. Tamilselvi, R. Anbarasan, Indian J. Sci. **1**, 6 (2012)

[51] H.E.I. Ghandoor, H.M. Zidan, M.H.K. Mostafa, M.I.M. Ismail, Int. J. Electrochem. Sci. **7**, 5734 (2012)

[52] K.F. Lin, H.M. Cheng, H.C. Hsu, L.J. Lin, W.F. Hsieh, Chem. Phys. Lett. **409**, 208 (2005)

[53] Milan P. Nikolic, Konstantinos P. Giannakopoulos, Dimosthenis Stamopoulos, Evagelia G. Moshopoulou, Vladimir V. Srdic, Mater. Res. Bull. **47**, 1513 (2012)

[54] M. Israelowitz, Thesis, Syracuse University, 2013

[55] F.P. Xavier, G.J. Goldsmith, Bull. Mater. Sci. **18**, 283 (1995)